Two-Step HNN-Based Pattern Recognition Combining DWT-Based Multi-Resolution Analysis for Rechargeable Cells Distinction

Seongjun Lee, *Member, IEEE*, and Jonghoon Kim, *Senior Member, IEEE*

***Abstract*—This article newly suggests two-step Hamming neural network (HNN)-based pattern recognition which combines the discrete wavelet transform (DWT)-based multi-resolution analysis (MRA) for providing an innovative and unique cell distinction. In contrast to the conventional methods, there are some remarkable features. First, the discharging/charging current signals (DCCSs) for reflecting load conditions with various dissimilar scenarios are used as representative patterns in the first-step HNN. Specifically, the usage of decomposed low- or high-frequency components (A_5/D_5) by the DWT-based MRA enables added characteristic parameters for providing the closest matches. Second, according to state-of-charge (SOC) range, especially in high SOC ranges, the allowable maximum charging currents in constant current/voltage (CC/CV) schemes are adjusted for avoiding over-charging. Third, the second-step HNN finally completes the recognition after closely matching several representative discharging/charging voltage signals applying the selected DCCS in the first step. Finally, simultaneous internal parameter extraction in the equivalent electrical circuit model during the second-step HNN provides useful information for verification of this article. Then, unnecessary experimental procedure and the time required for getting parameters of an arbitrary lithium-ion cell are abbreviated or reduced.**

***Index Terms*—Battery pack, cell distinction, discrete wavelet transform (DWT), Hamming neural network (HNN), multi-resolution analysis (MRA), pattern recognition.**

I. Introduction

With the abrupt growing interest in environmental risks owing to fossil fuels, renewable/rechargeable energy sources, especially lithium-ion cells, have been recognized as better alternatives [1]–[3]. The lithium-ion cells can be generally connected in series, parallel, and series/parallel for satisfying high-power and high-energy requirements of electric-powered transportations [electric vehicles and hybrid electric vehicles (HEVs)] and battery energy storage system [4], [5]. The most important thing to obtain an optimal discharging/charging condition in the above applications is to configure a battery pack that has less inner voltage/state-of-charge (SOC) imbalances among lithium-ion cells. However, some risks involved in cell manufacturing and architecture variability result in unavoidable cell-to-cell voltage/SOC differences in the battery pack [6]–[8]. For overcoming this problem, several studies of cell distinction and voltage/SOC equalization circuits (active/passive) before and after the occurrence of cell-to-cell variation have been simultaneously conducted [6]–[12]. Conventional approaches of cell distinction have the limitation of only applying a constant discharging/charging current profile in order to collect representative discharging/charging voltages of lithium-ion cells [9], [10]. Practically, it should be essential to improve the above-mentioned cell distinction because most current profiles have dissimilar scenarios including abrupt changes, different magnitudes, and the necessary time for discharging/charging that is dependent on the operating requirement of electric-powered transportation. Namely, several discharging/charging voltages based on different discharging/charging currents that reflect various load conditions are needed. Therefore, it is clear that an innovative and unique cell distinction that can overcome the above weaknesses in conventional cell distinction further provides some advantages, in terms of simplicity (uncomplicated), high efficiency, SOC/state-of-health (SOH) monitoring correctness, and guideline for stable battery pack configuration in the battery management system (BMS) [12].

The approach proposed in this study provides insight into the implementation of an innovative and unique cell distinction for the selection of lithium-ion cells that have similar electrochemical characteristics to lead the stable series/parallel battery pack and guarantee its safe discharging/charging. For this goal, this approach chose the Hamming neural network (HNN) to recognize discharging/charging current and its voltage patterns of lithium-ion cells [13]–[15], [17]. Specifically, for improving the performance on cell distinction compared to the above conventional researches, two-step HNN-based pattern recognition combining the discrete wavelet transform (DWT) is considered. Originally, experimental discharging/charging voltages of lithium-ion cells and their applied currents could be all assumed as original signals in the DWT [16], [18], [19]. These signals

Manuscript received August 25, 2019; revised January 11, 2020 and March 14, 2020; accepted April 6, 2020. Date of publication April 20, 2020; date of current version July 20, 2020. This work was supported by the Korea Institute of Energy Technology Evaluation and Planning (KETEP) grant funded by the Korea government (MOTIE) under Grant 20182410105280. Recommended for publication by Associate Editor Wenping Cao. *(Corresponding author: Jonghoon Kim.)*

Seongjun Lee is with the Department of Mechanical Engineering, Chosun University, Gwangju, South Korea (e-mail: lsj@chosun.ac.kr).

Jonghoon Kim is with the Department of Electrical Engineering, Chungnam National University, Daejeon, South Korea (e-mail: whdgns0422@cnu.ac.kr).

Color versions of one or more of the figures in this article are available online at http://ieeexplore.ieee.org.

Digital Object Identifier 10.1109/TPEL.2020.2989401

were, respectively, called the discharging/charging current signal (DCCS) and discharging/charging voltage signal (DCVS) of lithium-ion cells. Definitely, because of the non-stationary and transient phenomena of the DCCS and DCVS, there is no doubt that the DWT is the best solution to analyze the above-mentioned signals [20]–[25]. In particular, multi-resolution analysis (MRA) in the DWT has a vigorous function of both time and frequency localization [25]. Therefore, the DWT-based MRA performs filtering and down-sampling for decomposing original signals (in case of this study, DCCS) into time and frequency domains, respectively, focusing on short time intervals for high-frequency components (detail; D_n) and on long time intervals for low-frequency components (approximation; A_n) [25]. For this decomposition, a Daubechies wavelet with a basis of order three (dB3) having an orthogonality, which contributes to the classification disturbances and localization, is applied. According to the predetermined scale, the decomposition level is lastly determined as 5 [26], [27]. Thus, five respective approximations (A_1–A_5) and detail components (D_1–D_5) are obtained through the MRA. Among them, two components of approximation A_5 and detail D_5 are finally selected for applying characteristic parameters in the first-step HNN. As mentioned earlier, this approach applied the DCCS as an original signal in the DWT-based MRA. Given the decomposed components of A_5 and D_5, further information on $A_{5\,D}/A_{5\,C}$ and $D_{5\,D}/D_{5\,C}$ ($_D$: discharging, $_C$: charging) can be also obtained. Finally, a total of 26 characteristic parameters are applied in the first-step HNN. From statistical analysis for transforming binary patterns into 1 and -1 arrays, the first-step HNN is applied to identify the representative DCCS that most closely matches that of the arbitrary DCCS to be measured (input in the first-step HNN) [16]. For reference, a simple rule is performed a slight adjustment of the arbitrary DCCS scale for precise matching with a current scale of charging 6 A between discharging 6 A (-6 to 6 A) of 10 representative DCCSs. After the final selection of the representative DCCS and its usage, different discharging/charging voltages of 15 lithium-ion cells as representative DCVSs in the second-step HNN need to be considered, together with cell parameter measurement in the equivalent electrical circuit model (EECM) [28]. At this step, all DCVS patterns are separated into two sub-patterns of discharging voltage (DV) patterns and charging voltage (CVe) patterns to acquire seven characteristic parameters applied to the second-step HNN. The remaining procedure of this step is the same as that of the first step. By competitive learning of the so-called winner-take-all (WTA) network [15], [17], all final identification results, which are respectively the closest representative DCCS and DCVS patterns to each input pattern having only nonzero outputs at the first and second-step HNNs, are determined. Experimental results of the direct current internal resistance (DCIR), discharge capacity, and their comparison definitely validate the high-fidelity cell distinction based on two-step HNN-based pattern recognition. For this approach, some 18 650 cylindrical lithium-ion cells having a rated capacity of 2.6 Ah and a nominal voltage of 3.7 V have been efficiently conducted (ICR 18650-26F; Samsung SDI).

Fig. 1. Energy Storage System Lab and its experimental apparatus for implementation of this research.

The remainder of this article is organized as follows: It is divided into six sections, including this introduction section. The experimental apparatus for obtaining all DCCS/DCVS patterns and verifying the proposed approach is presented in Section II. A brief review of the theoretical backgrounds of the HNN and DWT is provided in Section III. Next, the first- and second-step HNNs separately considering representative DCCS and DCVS patterns are explained in Section IV. After discussing the feasibility of cell distinction, the summary and closing comments are given in Section V.

II. Experimental Apparatus for this Approach

The experimental apparatus for implementation of this approach in Energy Storage System Laboratory is shown in Fig. 1. As mentioned in Section I, experimental studies were conducted on 18 650 cylindrical lithium-ion cells that had a rated capacity of 2.6 Ah and a nominal voltage of 3.7 V (Samsung SDI). First, various scaled-down HEV current profiles were used to obtain the DCCSs for DWT-based MRA in the first-step HNN. Based on each DCCS, 15 lithium-ion cells having different electrochemical characteristics were experimented to obtain DCVSs [total DCCSs (10) $\times$ cells (15) $=$ DCVSs (150)]. This experimental apparatus was also used to measure the DCIR at SOC 50% and discharge capacity based on a fully charging–discharging scheme [constant current (CC)–CV protocol for charging, CC protocol for discharging] in order to verify this approach. Detailed information of our experimental apparatus shown in Fig. 1 is as follows. An electric load Hewlett Packard 6050A (60 V/50 A) for discharging and a power supply Agilent E3633A (20 V/10 A) for charging lithium-ion cells were used. The data acquisition board (general purpose interface bus communication) accurately collected and recorded data composed of

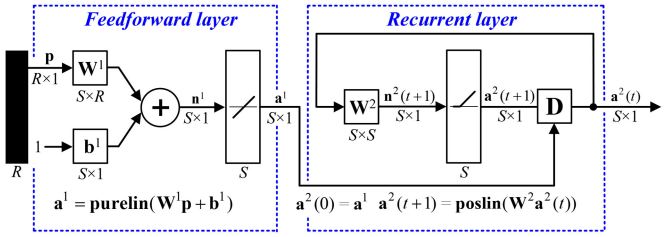

Fig. 2. Hamming neural network (HNN) having two layers, namely, feedforward layer and recurrent layer broadly used for pattern recognition.

discharging–charging current/voltage, Ah-counting based SOC, and temperature. These data were applied as input for our designed BMS controller established in MATLAB/Simulink S-function and C++. A self-made digital signal processor using STM32F105VC was utilized as a real-time BMS controller. All experiments were performed at a nominal temperature of 25 °C electronically controlled through an environmental/humidity chamber Hitachi U-6652P-CH3 for minimizing the cell temperature dependency.

III. Review of Hamming Neural Network (HNN) and Discrete Wavelet Transform (DWT)

A. Review of Hamming Neural Network (HNN)

The HNN shown in Fig. 2 is one of the simplest competitive networks for examining binary pattern recognition issues [13]–[15], [17]. By comparison of the inner products, this determines which representative pattern is nearest to the current pattern (prototype vector and input vector). There are two layers (feedforward layer and the recurrent layer) in the HNN. The role of the feedforward layer is to calculate an inner product and a correlation between each prototype vector and an input vector for finding the minimum Hamming distance (HD) from the difference calculation between the dimension m and HD. A set of prototype vectors of weight matrix $\mathbf{W}^1$ in (1) and bias vectors $\mathbf{b}^1$ in (2) is transformed into the binary form [13], [14]. Each prototype vector in matrix $\mathbf{W}^1$ is needed to be recognized with $m/2$ as each component. $\mathbf{b}^1$ is the threshold value given in the number R of each input vector and the neuron's number S. Between vectors ${}_i\mathbf{w}$ and a given input vector $\mathbf{p}$, HD(${}_i\mathbf{w}$, $\mathbf{p}$) has influence on the $\mathbf{W}^1\mathbf{p}$ as in$\mathbf{W}^1\mathbf{p} = [m - HD({}_i\mathbf{w}, \mathbf{p})] - HD({}_i\mathbf{w}, \mathbf{p})$ at an arbitrary node i ($1 \le I \le R$). As expressed in (3), the outputs $\mathbf{a}^1$ of the feedforward layer are identical to the inner products $\mathbf{p}_S^T\mathbf{p}$ by implementing a linear transfer function (**purelin**) plus R [13]. The prototype vector that is closest in HD to the input vector has the largest output $\mathbf{a}^1$ in this layer. After initialization [$\mathbf{a}^2(0) = \mathbf{a}^1$] of the outputs of the feedforward layer, a competitive layer or MAXNET, namely, the recurrent layer that performs the WTA operation, is used for the purpose of the ith node's initial dominant response enhancement and suppression of other nodes. Equation (4) expresses the $n \times n$ weight matrix of the recurrent layer $\mathbf{W}^2$ that has two kinds of weights including the diagonal elements 1 and the off-diagonal elements having a small negative value $-\varepsilon$ with a range of $0 < \varepsilon < 1/(S-1)$ where $1 \le I \le S$ and $1 \le j \le S$ [13]. Contrary to the feedforward layer, this layer implements a positive transfer function (**poslin**) for recurrent processing and frequent updating (namely WTA) of output $\mathbf{a}^2$ until a final winner decision is made. Then, this final winner only has a positive output at the ith node, whereas all remaining nodes decay to zero. Consequently, this indicator of the recurrent layer vector having only a positive output is the representative vector that is the best match with the input [13].

Main equations of HNN

<*Feedforward layer*>

$$\mathbf{W}^1 = \begin{bmatrix} {}_1\mathbf{w}^{iT} \\ {}_2\mathbf{w}^{iT} \\ \vdots \\ {}_S\mathbf{w}^{iT} \end{bmatrix} = \frac{1}{2}\begin{bmatrix} {}_1\mathbf{w}^1 & {}_2\mathbf{w}^1 & \cdots & {}_S\mathbf{w}^1 \\ {}_1\mathbf{w}^2 & {}_2\mathbf{w}^2 & \cdots & {}_S\mathbf{w}^2 \\ \vdots & \vdots & \ddots & \vdots \\ {}_1\mathbf{w}^R & {}_2\mathbf{w}^R & \cdots & {}_S\mathbf{w}^R \end{bmatrix}^T = \begin{bmatrix} \mathbf{p}_1^T \\ \mathbf{p}_2^T \\ \vdots \\ \mathbf{p}_S^T \end{bmatrix} \tag{1}$$

$$\mathbf{b}^1 = [R,\ R,\ \ldots,\ R]^T = \left[\frac{m}{2}, \frac{m}{2}, \ldots, \frac{m}{2}\right]^T \tag{2}$$

$$\mathbf{a}^1 = \mathbf{W}^1\mathbf{p} + \mathbf{b}^1 = \begin{bmatrix} \mathbf{p}_1^T\mathbf{p} + R & \cdots & \mathbf{p}_S^T\mathbf{p} + R \end{bmatrix}^T = \mathbf{purelin}(\mathbf{W}^1\mathbf{p} + \mathbf{b}^1). \tag{3}$$

<*Recurrent layer*>

$$\mathbf{W}^2 = \begin{bmatrix} {}_1\mathbf{w}^1 & {}_1\mathbf{w}^2 & \cdots & {}_1\mathbf{w}^S \\ {}_2\mathbf{w}^1 & {}_2\mathbf{w}^2 & \cdots & {}_2\mathbf{w}^S \\ \vdots & \vdots & \ddots & \vdots \\ {}_i\mathbf{w}^1 & {}_i\mathbf{w}^2 & \cdots & {}_i\mathbf{w}^S \end{bmatrix} = \begin{bmatrix} 1 & -\varepsilon & \cdots & -\varepsilon \\ -\varepsilon & 1 & \cdots & -\varepsilon \\ \vdots & \vdots & \ddots & \vdots \\ -\varepsilon & -\varepsilon & \cdots & 1 \end{bmatrix} \tag{4}$$

$$\mathbf{a}_i^2(t+1) = \mathbf{poslin}(\mathbf{W}^2\mathbf{a}_i^2(t)) = \mathbf{poslin}\left(\mathbf{a}_i^2(t) - \varepsilon\sum_{j\neq i}\mathbf{a}_j^2(t)\right). \tag{5}$$

Main equations of DWT

$$DWT(j,k) = \frac{1}{\sqrt{2^j}}\int_{-\infty}^{\infty} x(t)\psi^*\left(\frac{t-k2^j}{2^j}\right)dt \tag{6}$$

$$\phi_{j,k}(t) = 2^{-\frac{j}{2}}\phi(2^{-j}t - k), \quad \psi_{j,k}(t) = 2^{-\frac{j}{2}}\psi(2^{-j}t - k) \tag{7}$$

$$\phi_{j,k}(t) = \sqrt{2}\sum_n h(n)\phi(2t-n) \quad \psi_{j,k}(t) = \sqrt{2}\sum_n g(n)\phi(2t-n) \tag{8}$$

$$a_{j,k} \le x(t), \phi_{j,k}(t) \ge \sum_n h(n-2k)a_{j-1,n} \tag{9}$$

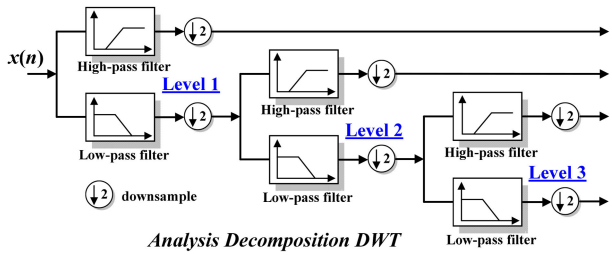

Fig. 3. Discrete wavelet transform (DWT)-based three-level multi-resolution analysis (MRA) for analysis decomposition.

$$d_{j,k} \leq x(t), \psi_{j,k}(t) \geq \sum_{n} g(n-2k)a_{j-1,n} \tag{10}$$

$$x(t) = \sum_{k=0}^{2^{N-j}-1} a_{j,k} 2^{-\frac{j}{2}} \phi(2^{-j}t-k) + \sum_{j=1}^{J} \sum_{k=0}^{2^{N-j}-1} d_{j,k} 2^{-\frac{j}{2}} \psi(2^{-j}t-k). \tag{11}$$

B. Review of Discrete Wavelet Transform (DWT)

The DWT has been broadly researched and implemented for a new mathematical theory that decomposes a nonstationary time-domain signal into different frequency groups in contrast to the Fourier transform [16], [18]–[27]. Some merits of the DWT are that it operates only in discrete steps, has a high reduction in the computational time, and provides sufficient useful information for signal analysis. A basic equation for defining the DWT is expressed in (6) with the mother wavelet $\psi(t)$, dilation scaling parameter j, and translation scaling parameter k. Then, each role of the above parameters determines the wavelet's length/oscillatory frequency and its shifted position. Based on the above terms, a dyadic-orthonormal wavelet transform is used as the basis of the MRA. In this MRA process shown in Fig. 3, an original signal $x(t)$ can be fully decomposed with respect to approximations/details respectively provided by the scaling function $\phi_{j,k}(t)$ and the wavelet function $\psi_{j,k}(t)$ shown in (7) (integer j and k). Low- and/or high-pass filter coefficients of $h(n)$ and $g(n)$, respectively, correlate the scaling/wavelet functions that satisfy $g(L-1-n) = (-1)^n h(n)$. From these filter coefficients, two functions of $\phi_{j,k}(t)$ and $\psi_{j,k}(t)$ in (7) can be additionally expressed in (8) for the construction of each filters [16]. The MRA shown as a set of successive filter banks in Fig. 4 decomposes an original signal $x(t)$ into low (approximation A_n) and high (detail D_n) frequency components via the approximate/detailed coefficients of $a_{j,k}$ and $d_{j,k}$ [(8) and (9); level j]. Given decomposition level J and $x(t)$'s length N ($J \leq N$), (10) expresses the J-level DWT representation with wavelet transform coefficients ($1 \leq j \leq J$) [18]. Specifically, the sampling frequency f_s of an original signal $x(t)$ plays a significant role in finding a suitable decomposition level by the Nyquist criterion. A comprehensive detail component D_n has information in terms of the signal components with frequency interval $[2^{-(n+1)}f_s, 2^{-n}f_s]$ Hz [18].

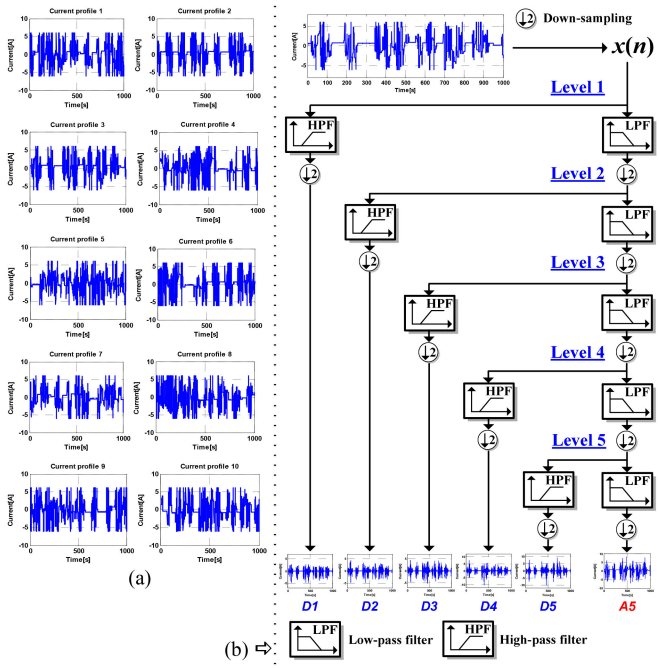

Fig. 4. Preparation for first-step HNN-based pattern recognition. (a) Ten different discharging/charging current signals (DCCSs) within range (−6 to 6 A). (b) DWT-based MRA considering five decomposition levels.

By contrast, within the interval $[0, 2^{-(n+1)}f_s]$, a generic approximation component A_n containing the low-frequency component is finally determined [18].

IV. Proposed Approach

A. First-Step HNN-Based Pattern Recognition (DCCS Info.)

Most discharging/charging currents applied to lithium-ion rechargeable cells have different schemes of abrupt change, time required for discharging/charging, and current's magnitude. For that reason, it should be surely required to assume these currents as signals, in other words the DCCS, and to distinguish each DCCS' principal features. For reference, this research used cylindrical 18 650 cylindrical lithium-ion cells having a rated capacity of 2.6 Ah; thus, it is required to adjust the scale of all DCCSs to prevent the cell's internal damage owing to over-discharging/over-charging. This is why our study prepared 10 scaled-down DCCSs of the HEVs within the range of −6 to 6 A applied during 1000 s, as shown in Fig. 4(a). These DCCSs were decomposed into two components such as approximation A_n (for a long time interval) and detail D_n (for a short time interval) by the DWT. For the MRA implementation, it was previously required to select an optimum wavelet function (mother wavelet) for better decomposition of an original signal. Among various mother wavelets of Haar, Coiflet, Biorthogonal, Daubechies, Symlet, Morlet, etc., this approach finally selected the Daubechies wavelet with orthogonality and potentiality for achieving localization and disturbance classification [19]. Next, two additional items (basis order of the mother wavelet and decomposition level) should be clearly set. Because of slight

TABLE I
FREQUENCY BANDS OBTAINED BY DECOMPOSITION AT MULTIPLE LEVELS

Level No.	Wavelet decomposition	Component type	Frequency bands (Hz)
1	D_1	Detail	250~500 ($f_s/2^2$~ $f_s/2^1$) Hz
2	D_2	Detail	125~250 ($f_s/2^3$~ $f_s/2^2$) Hz
3	D_3	Detail	62.5~125 ($f_s/2^4$~ $f_s/2^3$) Hz
4	D_4	Detail	31.25~62.5 ($f_s/2^5$~ $f_s/2^4$) Hz
5	D_5	Detail	15.625~31.25 ($f_s/2^6$~ $f_s/2^5$) Hz
5	A_5	Approximation	0~15.625 (0~ $f_s/2^6$) Hz

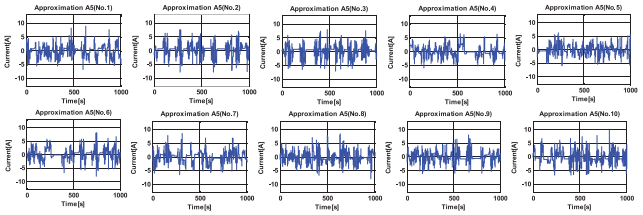

Fig. 5. Ten different approximation components A_5 decomposed by DWT-based MRA considering five decomposition levels from ten DCCSs.

differences in decomposition performance related to localization and disturbance classification in the DWT, the dB3 is randomly chosen based on [19]–[21]. In contrast to the wavelet's basis order, the level n for decomposition is primarily dependent on the sampling frequency f_s for capturing the DCCSs and the supply frequency f for collecting precise experimental results. Considering three values of f_s, f, and n, the equation of $2^{(-n+1)}f_s < f$ was defined in [22] and [23]. If the supply frequency f is included in detail component D_n, the approximation component of this level A_n only contains signal components with frequencies below f. This frequency can be defined as 20 Hz because of a 50-ms time interval previously set for the precise collection of experimental results in this article. According to two values $f_s = 1000$ sample/s and $f = 20$ Hz (50 ms), the decomposition level n can be calculated as 5 in (12) and the data window size as $32(=2^5)$

$$n = \text{Integer}\left[\log\left(f_s/f\right)/\log\left(2\right)\right] = 5. \tag{12}$$

Through the decomposition level $n = 5$, the DWT-based MRA carries out filtering and down-sampling $\downarrow 2$ for decomposing all DCCSs in order to create five approximation (A_1–A_5) and five detail components (D_1–D_5) using approximate $a_{j,k}$ and detail coefficients $d_{j,k}$, respectively. Then, as shown in Fig. 4(b), the lowest frequency band A_5 and high-frequency bands D_1–D_5 are finally chosen from the above components. Table I lists each frequency bands obtained by decomposition in five levels by applying a data window of 32 samples with $f_s = 1000$ sample/s. Specifically, because of the predetermined value $n = 5$ in (12), in this approach, two components (A_5 and D_5) are selected from all approximation and detail components as characteristic parameters in the HNN. As shown in Figs. 5 and 6, by the DWT-based MRA, 10 DCCSs can be decomposed into each approximation A_5 and detail D_5 components. Further information on $A_{5\,D}$/$A_{5\,C}$ and $D_{5\,D}$/$D_{5\,C}$ based on the initial starting voltage points (ISVP) fixations ($_D$: discharging; $_C$: charging) are

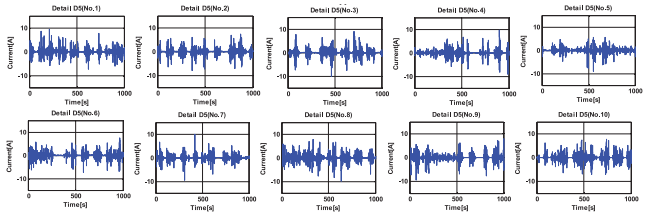

Fig. 6. Ten different detail components D_5 decomposed by DWT-based MRA considering five decomposition levels from ten DCCSs.

TABLE II
TWENTY-SIX CHARACTERISTIC PARAMETERS USED IN FIRST-STEP HNN

	Approximation component A_5		Detail component D_5
C_f1	Average A_5	C_f14	Average D_5
C_f2	Standard deviation A_5	C_f15	Standard deviation D_5
C_f3	Maximum A_5	C_f16	Maximum D_5
C_f4	Minimum A_5	C_f17	Minimum D_5
C_f5	A_5<1A (Absolute value) average	C_f18	D_5<0.001A (Abs.×10000) avg.
C_f6	A_5<1A (Absolute value) std.	C_f19	D_5<0.001A (Abs.×1000) std.
C_f7	A_5<1A (Absolute value) duration	C_f20	D_5<0.001A (Abs.) duration
C_f8	Average A_{5D} (discharge)	C_f21	Average D_{5D} (discharge)
C_f9	Standard deviation A_{5D} (disch.)	C_f22	Standard deviation D_{5D} (disch.)
C_f10	Duration time A_{5D} (discharge)	C_f23	Duration time D_{5D} (discharge)
C_f11	Average A_{5C} (charge)	C_f24	Average D_{5C} (charge)
C_f12	Standard deviation A_{5C} (charge)	C_f25	Standard deviation D_{5C} (charge)
C_f13	Duration time A_{5C} (charge)	C_f26	Duration time D_{5C} (charge)

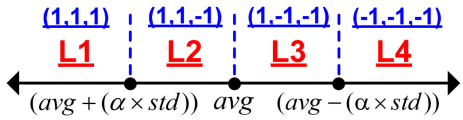

Fig. 7. Four levels for three standards for transforming into 1 and −1 arrays.

obtained [9]. Various information such as the average, standard deviation, maximum/minimum, and duration time can be applied as characteristic parameters in the HNN, namely, C_f1–C_f13 and C_f14–C_f26, respectively, which are A_5 and D_5 ($_f$: first). A total of 26 characteristic parameters (C_f1–C_f26) are introduced in Table II. Through four levels and three standards displayed in Fig. 7, each value of the 26 characteristic parameters that correspond to 10 representative DCCSs is transformed into 1 and −1 arrays (avg: average; std: standard deviation; $\alpha = 0.5$). Four levels (L1–L4) from the above values transformed into binary form are well listed in Table III. Three standards, which are [avg − (α × std), avg, and avg + (α × std)], determine each level. After determining avg and std of each characteristic parameter of the 10 representative DCCSs, the value of any DCCS is compared with the above three standards for a level decision. For example, in the case of C_f3 of Pro.6 (maximum A_5 of current profile 6), the level is L2. This means the value of C_f3 of Pro.6 is smaller than avg and larger than avg + (α × std). For reference, in order to consider the marked differences of the 10 DCCSs, the tuning value α is chosen as 0.5. Fig. 8 shows the HNN structure for DCCS pattern recognition in the first-step. This figure represents the feedforward's role as calculating the inner product between each representative and the current DCCS patterns. Considered in $\mathbf{b}^1 = [78, 78, \ldots, 78]^T$ in Fig. 8, the

TABLE III
TWENTY-SIX CHARACTERISTIC PARAMETERS OF TEN REPRESENTATIVE DCCS PATTERNS

	Pro.1	Pro.2	Pro.3	Pro.4	Pro.5	Pro.6	Pro.7	Pro.8	Pro.9	Pro.10
C_f1	L4	L1	L1	L2	L4	L1	L3	L4	L4	L4
C_f2	L1	L1	L3	L4	L4	L2	L2	L2	L4	L1
C_f3	L1	L3	L3	L4	L4	L2	L2	L2	L3	L1
C_f4	L3	L4	L3	L1	L1	L4	L1	L4	L1	L2
C_f5	L1	L1	L1	L4	L4	L2	L2	L4	L4	L4
C_f6	L2	L4	L4	L4	L2	L2	L1	L1	L1	L2
C_f7	L4	L1	L1	L1	L3	L2	L4	L4	L1	L4
C_f8	L4	L4	L1	L1	L3	L2	L3	L1	L2	L1
C_f9	L4	L4	L2	L2	L4	L1	L2	L2	L2	L1
C_f10	L2	L1	L4	L4	L4	L2	L2	L4	L4	L4
C_f11	L3	L4	L1	L1	L1	L1	L3	L2	L1	L1
C_f12	L2	L1	L4	L4	L4	L2	L2	L3	L4	L4
C_f13	L3	L4	L1	L1	L1	L3	L3	L1	L1	L1
C_f14	L1	L4	L1	L1	L4	L4	L4	L1	L1	L1
C_f15	L1	L2	L3	L3	L4	L3	L4	L1	L2	L1
C_f16	L1	L4	L1	L1	L4	L3	L1	L3	L4	L3
C_f17	L1	L1	L3	L3	L3	L1	L4	L4	L4	L1
C_f18	L1	L3	L2	L2	L3	L4	L1	L4	L2	L1
C_f19	L4	L3	L1	L1	L2	L2	L4	L1	L2	L4
C_f20	L3	L1	L3	L3	L4	L1	L1	L4	L3	L3
C_f21	L1	L3	L4	L4	L4	L2	L4	L1	L2	L1
C_f22	L1	L3	L3	L3	L4	L4	L4	L1	L3	L1
C_f23	L1	L3	L1	L1	L4	L4	L1	L4	L4	L3
C_f24	L4	L2	L1	L1	L1	L2	L1	L4	L2	L4
C_f25	L2	L2	L3	L3	L4	L3	L4	L1	L1	L1
Cf26	L4	L2	L4	L4	L1	L1	L4	L1	L1	L2

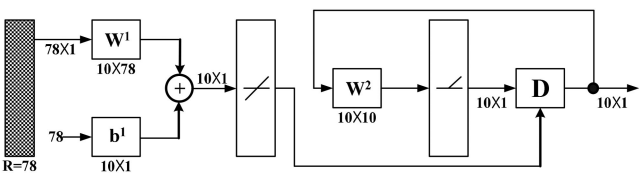

Fig. 8. HNN structure for DCCS pattern recognition in the first-step HNN.

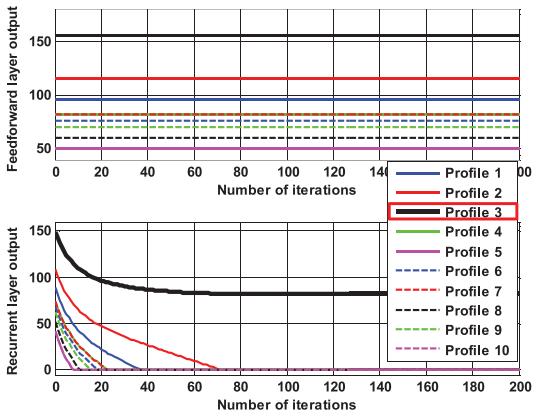

Fig. 9. Outputs of feedforward layer and recurrent layer in the first-step HNN [selected DCCS: Pro.3 (current profile 3)].

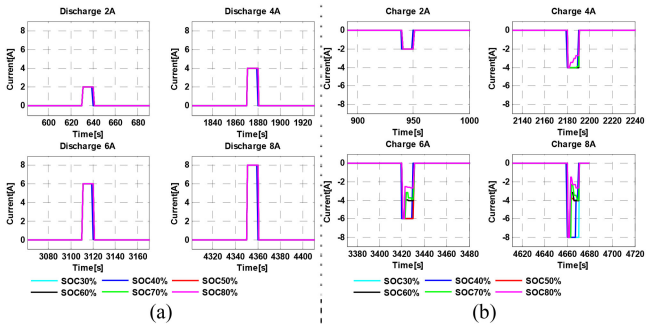

Fig. 10. Scaling up and down of discharging/charging currents at six points of SOC for learning HNN. (a) Discharging. (b) Charging.

weight matrix $\mathbf{W}^1$ stores the binary form previously transformed from the value of each of the 26 characteristic parameters corresponding to 10 representative DCCSs [see (13)]. For a given input vector $\mathbf{p}$ in the feedforward layer, the 10 neurons storing the results of the inner product compete with each other to determine a winner. This WTA needs self-feedback connection and negative lateral inhibition connection. There are two kinds of weights in the recurrent layer $\mathbf{W}^2$: Diagonal element 1 and off-diagonal elements having a small negative value, where $0 < \varepsilon < 1/(10-1)$ is called the lateral interaction coefficient ($\varepsilon = 0.05$) as expressed in (14). By this competition, it can be shown that only one neuron with a nonzero output indicates the representative DCCS, which is closest to an arbitrary DCCS pattern [Fig. 9; selected DCCS (Pro.3)]

$$\mathbf{W}^1 = \begin{bmatrix} {}_1\mathbf{w}^{iT} \\ {}_2\mathbf{w}^{iT} \\ \vdots \\ {}_{10}\mathbf{w}^{iT} \end{bmatrix} = \frac{1}{2}\begin{bmatrix} {}_1\mathbf{w}^1 & {}_2\mathbf{w}^1 & \cdots & {}_{10}\mathbf{w}^1 \\ {}_1\mathbf{w}^2 & {}_2\mathbf{w}^2 & \cdots & {}_{10}\mathbf{w}^2 \\ \vdots & \vdots & \ddots & \vdots \\ {}_1\mathbf{w}^{78} & {}_2\mathbf{w}^{78} & \cdots & {}_{10}\mathbf{w}^{78} \end{bmatrix}^T = \begin{bmatrix} \mathbf{p}_1^T \\ \mathbf{p}_2^T \\ \vdots \\ \mathbf{p}_{10}^T \end{bmatrix} \tag{13}$$

$$\mathbf{W}^2 = \begin{bmatrix} {}_1\mathbf{w}^1 & {}_1\mathbf{w}^2 & \cdots & {}_1\mathbf{w}^{10} \\ {}_2\mathbf{w}^1 & {}_2\mathbf{w}^2 & \cdots & {}_2\mathbf{w}^{10} \\ \vdots & \vdots & \ddots & \vdots \\ {}_{10}\mathbf{w}^1 & {}_{10}\mathbf{w}^2 & \cdots & {}_{10}\mathbf{w}^{10} \end{bmatrix} = \begin{bmatrix} 1 & -0.05 & \cdots & -0.05 \\ -0.05 & 1 & \cdots & -0.05 \\ \vdots & \vdots & \ddots & \vdots \\ -0.05 & -0.05 & \cdots & 1 \end{bmatrix}. \tag{14}$$

For reference, the first-step HNN considered all DCCSs with identical discharging/charging current range of -6 to 6 A for learning. Thus, it is required to adjust the scale of the above current range because an arbitrary DCCS used as an input of the first-step HNN may have a different range than that of all representative DCCSs. In the case of discharging, there is little possibility of reaching the discharge cutoff voltage (2.8 V). Thus, regardless of current magnitude, it is possible to obtain the adjusted current scaled up or down from an arbitrary DCCS by the ratio between 10 representative DCCSs in Fig. 4(a) and an arbitrary DCCS at SOC 30%–80%, as shown in Fig. 10(a). In contrast to the discharging condition, it is not easy to adopt the

TABLE IV
CC-CV CHARGING METHOD INFLUENCED BY CURRENT MAGNITUDES/SOC RANGES AND ALLOWABLE MAXIMUM CHARGING CURRENT

	30%	40%	50%	60%	70%	80%
1A	CC	CC	CC	CC	CC	CC
2A	CC	CC	CC	CC	CC	CC
3A	CC	CC	CC	CC	CC	CV 2.8809A
4A	CC	CC	CC①	CC	CV 3.8885A	CV 3.4894A
5A	CC	CC	CC	CC	CV 3.8915A	CV 2.9831A
6A	CC	CC	CC	CV② 4.0021A	CV 3.9042A	CV 2.6577A
7A	CC	CC	CV 4.0084A	CV 4.0050A	CV 3.9123A	CV 2.6601A
8A	CC	CV 4.0138A	CV 4.0090A	CV 4.0078A	CV 3.9561A	CV 2.6607A

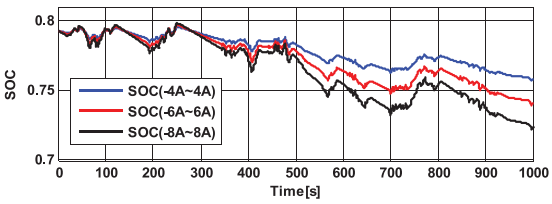

Fig. 11. SOC variances with different current magnitudes.

above rule in the charging condition because the charge cutoff voltage (4.2 V) is reached with increased current magnitudes in high SOC range. As shown in Fig. 10(b), there is no difficulty in scaling up and down with decreased current magnitudes in low SOC ranges. However, the CV scheme in the charging condition, especially in high SOC ranges, surely needs decreased currents in order to avoid an overvoltage that causes internal damage inside a lithium-ion cell. For this reason, as listed in Table III, the allowable maximum charging currents in the CC/CV schemes were partly changed (in case of the CV scheme) and used in the first-step HNN. For example, if an arbitrary current profile within 4 A is applied at SOC 50%, its adjustment properly scaled up/down for precise matching with a current scale (−6 to 6 A) is used as a new input in the first-step HNN (1.5 times; ① in Table III). However, for SOC 60%, especially above a current magnitude of 5 A, the CV scheme should be applied in order to avoid cell over-charging. Thus, the allowable maximum charging current is limited to 4.0021 A (② in Table III) based on preliminary experimental results. Each allowable maximum charging current based on the variable current magnitudes/SOC ranges is listed in Table III. Irrespective of current magnitudes and SOC ranges, it is unnecessary to scale up and down the magnitude of the discharging current (all CC regimes). Through a scaled up/down current, it is shown that there is clear SOC variance, as shown in Fig. 11. Assumed in few parameter changes in EECM [28], it is not difficult to obtain the adjusted terminal voltage by only considering the SOC information dependent on the magnitude of the scaled up/down current. Finally, this adjusted voltage is subsequently used as a new input (DCVS) in the second-step HNN-based pattern recognition introduced in Section IV-B.

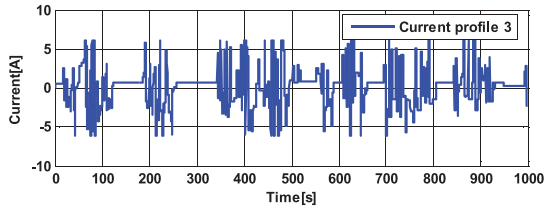

Fig. 12. Current profile of selected DCCS in the first-step HNN (Pro.3).

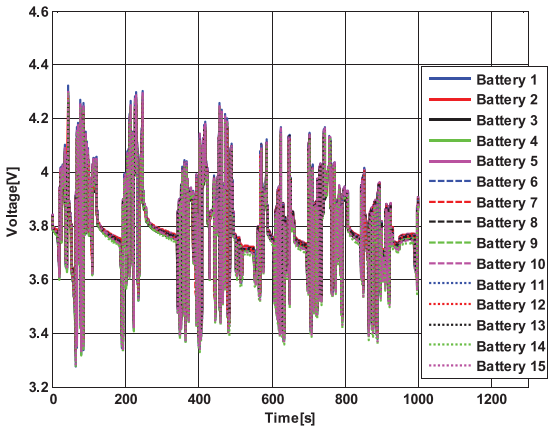

Fig. 13. Fifteen representative DCVSs with current profile (Pro.3) finally selected in the first-step HNN.

TABLE V
SEVEN CHARACTERISTIC PARAMETERS USED IN THE SECOND-STEP HNN

C_s1	DCVS	Standard deviation DCVS
C_s2	DV	Standard deviation DV
C_s3	CV	Standard deviation CV
C_s4	DV	Average DV (ISVP consideration)
C_s5		Standard deviation DV (ISVP consideration)
C_s6	CV	Average CV (ISVP consideration)
C_s7		Standard deviation CV (ISVP consideration)

B. Second-Step HNN-Based Pattern Recognition (DCVS Info.)

After final selection of the current profile (Pro.3) as a representative DCCS pattern closest to an arbitrary DCCS pattern in the first-step HNN and its scaled up/down value (see Fig. 12), it is required to get 15 different representative DCVSs, together with cell parameter measurements in EECM based on the above profile as shown in Fig. 13. At this step, in order to perform the second-step HNN (current information i), all DCVS patterns are divided into two sub-patterns including DV ($I \geq 0$) and CVe ($I < 0$). Next, based on the ISVP fixation that minimizes initial starting voltage differences among DVs and CVes in Fig. 14 [16], seven characteristic parameters applied in the second-step HNN can be finally set, together with the DCVS (C_s1–C_s7). Simple information such as the average and standard deviation of DVs/CVes are considered as seven characteristic parameters (Table IV). Fortunately, the remaining procedure of this second-step HNN is identical to that of the first-step HNN. Fig. 15 shows a graphic of 1 and −1 arrays previously transformed from each value of the seven characteristic parameters (C_s1–C_s7 listed in Table V) corresponding to 15 representative DCVS

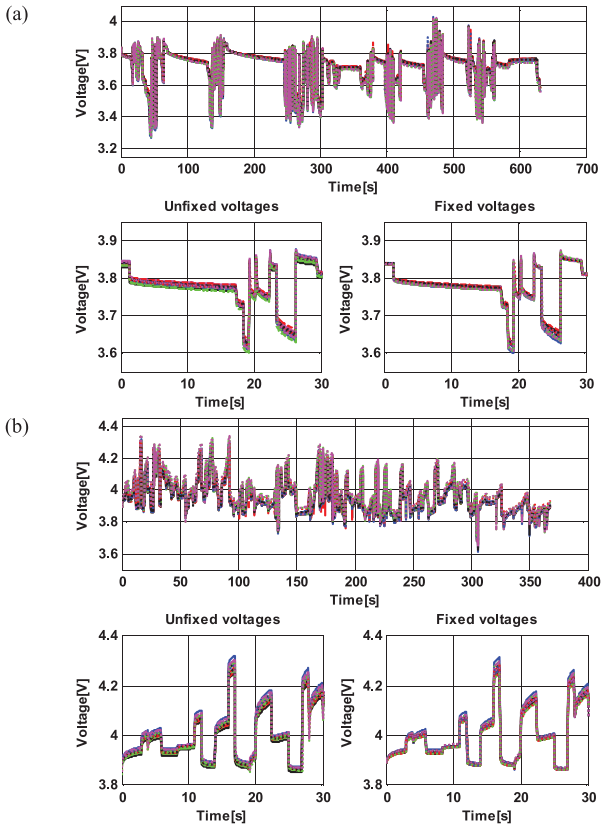

Fig. 14. Unfixed/fixed (after ISVP) discharging voltages (DV) (current ≥ 0) and charging voltages (CVe) patterns (current < 0) previously separated from 15 representative DCVSs (from Pro.3). (a) Discharging. (b) Charging.

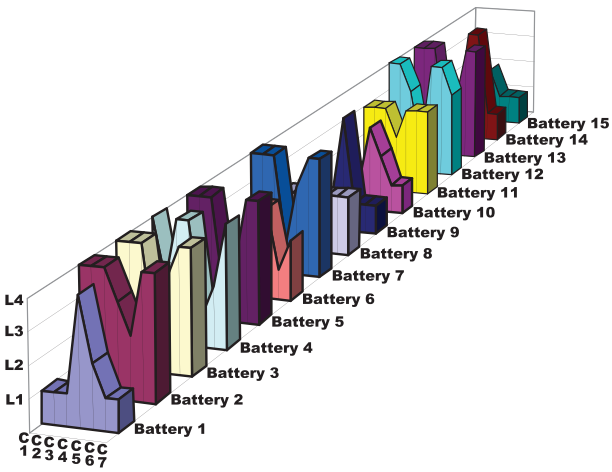

Fig. 15. Characteristic level of 15 representative DCVS patterns in the second-step HNN.

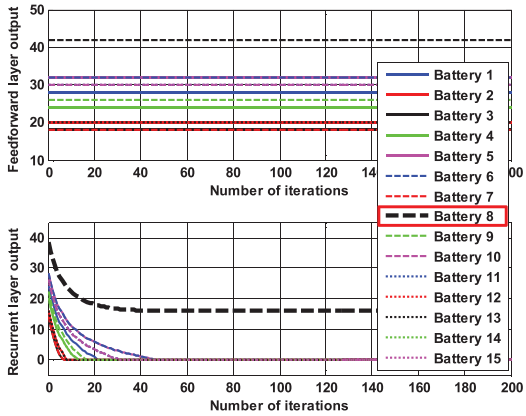

Fig. 16. Final outputs of feedforward layer and recurrent layers in the second-step HNN (selected DCVS having a nonzero output: Battery 8).

According to the WTA network [15], it is capable of selecting the DCVS pattern that has a nonzero output in the recurrent layer. This output means there is little electrochemical differences between the selected and arbitrary DCVS patterns (closest). In Fig. 16, after the competition in the recurrent layer, we can conclude that the representative DCVS pattern is Battery 8, which is closest to an arbitrary DCVS input pattern in the second-step HNN. The procedure that involves the two-step HNN-based pattern recognition proposed in this approach (Fig. 17)

$$\mathbf{W}^1 = \begin{bmatrix} {}_1\mathbf{w}^{iT} \\ {}_2\mathbf{w}^{iT} \\ \vdots \\ {}_{15}\mathbf{w}^{iT} \end{bmatrix} = \frac{1}{2}\begin{bmatrix} {}_1\mathbf{w}^1 & {}_2\mathbf{w}^1 & \cdots & {}_{15}\mathbf{w}^1 \\ {}_1\mathbf{w}^2 & {}_2\mathbf{w}^2 & \cdots & {}_{15}\mathbf{w}^2 \\ \vdots & \vdots & \ddots & \vdots \\ {}_1\mathbf{w}^{21} & {}_2\mathbf{w}^{21} & \cdots & {}_{15}\mathbf{w}^{21} \end{bmatrix}^T = \begin{bmatrix} \mathbf{p}_1^T \\ \mathbf{p}_2^T \\ \vdots \\ \mathbf{p}_{15}^T \end{bmatrix} \tag{15}$$

$$\mathbf{W}^2 = \begin{bmatrix} {}_1\mathbf{w}^1 & {}_1\mathbf{w}^2 & \cdots & {}_1\mathbf{w}^{15} \\ {}_2\mathbf{w}^1 & {}_2\mathbf{w}^2 & \cdots & {}_2\mathbf{w}^{15} \\ \vdots & \vdots & \ddots & \vdots \\ {}_{15}\mathbf{w}^1 & {}_{15}\mathbf{w}^2 & \cdots & {}_{15}\mathbf{w}^{15} \end{bmatrix} = \begin{bmatrix} 1 & -0.05 & \cdots & -0.05 \\ -0.05 & 1 & \cdots & -0.05 \\ \vdots & \vdots & \ddots & \vdots \\ -0.05 & -0.05 & \cdots & 1 \end{bmatrix}. \tag{16}$$

patterns based on the rule of Fig. 7. Due to the number of changes in the representative DCVS pattern (10(f) $\Rightarrow$15(s)) and characteristic parameters [26(f) $\Rightarrow$ 7(s)], it is shown that (13) and (14) are, respectively, changed to (15) and (16) (f: first; s: second). Modified equations and $\mathbf{b}^1 = [21, 21, \ldots, 21]^T$ are newly applied in the HNN structure displayed in Fig. 8.

Verification of this approach is provided according to a comparison of cell parameter information such as the discharge capacity and DCIR between an arbitrary input and 15 representative lithium-ion cells. Fig. 18 shows the cell distinction among 15 representative lithium-ion cells with similar values of discharge capacity and DCIR when compared to those of an arbitrary

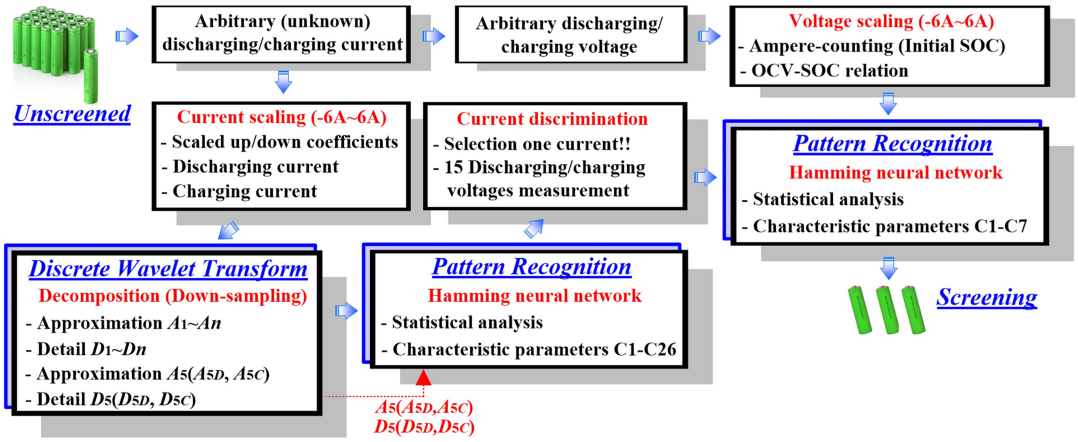

Fig. 17. Schematic diagram of proposed approach.

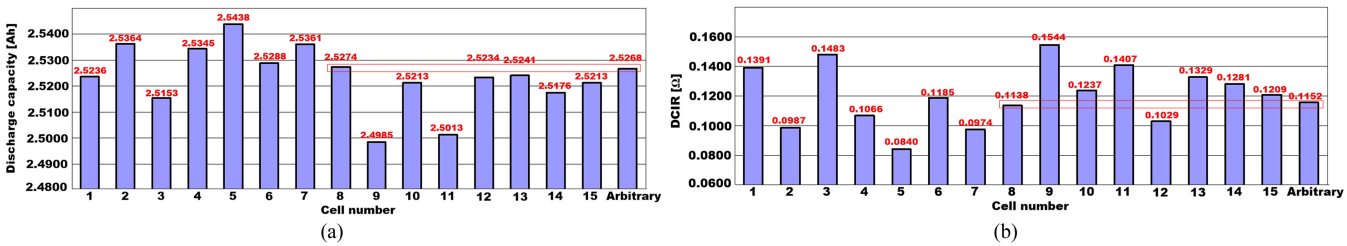

Fig. 18. Cell distinction among 15 representative lithium-ion cells with similar discharge capacities and DCIRs compared to those of arbitrary lithium-ion cell (input in the second-step HNN). (a) Discharge capacity. (b) DCIR.

lithium-ion cell. From Fig. 18, among marked differences for 15 lithium-ion cells, the final cell determined by this approach is Battery 8 (No. 8), which has 2.5274 Ah and 0.1138 Ω. It is actually checked that an arbitrary lithium-ion cell has two values of 2.5268 Ah and 0.1152 Ω.

C. Additional Discussion

This article started using only 10 current profiles (DCCS) and 15 lithium-ion cells (DCVS) in the first- and second-step HNN. Of course, the increased numbers of current profiles and lithium-ion cells in the HNN are welcome to improve the correctness of cell distinction. However, the most important task is to succeed our objective, high-fidelity cell distinction under limited current profiles and number of lithium-ion cells. Regardless of the discharging/charging condition with various sequences, this research is expected to provide more impressive distinction for selecting cells with similar electrochemical characteristics.

Contrary to the conventional methods for cell distinction, this research has some advantages.

1) Unnecessary experimental procedure and time for obtaining internal parameters (namely parameters identification) applied in the EECM of an arbitrary lithium-ion cell is possible. From this, it can be expected to have high-accuracy SOC estimation and SOH prediction in the BMS (EECM-based SOC/SOH monitoring via adaptive methods).

2) It is capable of configuring the stable/safe battery pack through more sophisticated cell distinction. The minimization of cell-to-cell voltage/SOC imbalances and less consideration in balancing circuit for electric-powered application for high-accuracy BMS are possible.

3) The usage of various DCCSs with different discharging/charging sequences in the first-step HNN is to provide the convenience of usage of nonstandard and reduction of the time required for obtaining DCCSs.

4) According to the similarity check between the DCCS patterns and an arbitrary input current, there is little difficulty in reducing the time required for performing the first-step HNN-based pattern recognition.

5) If lithium-ion cell's experimental voltages at various temperatures are applied in the second-step HNN-based pattern recognition, sensorless temperature monitoring or estimation of cell's operating temperature is practicable and definitely leads to the cost-effective BMS.

6) The size reduction (uncomplicated) of the BMS for SOH prediction is possible. Through considering aged lithium-ion cell's experimental voltage in the second-step HNN, from matching results of the resistance and discharge capacity, it is possible to predict the lithium-ion cell's degradation without complicated EECM-based methods [e.g., dual extended Kalman filter based SOC/SOH monitoring ⇒ extended Kalman filter based SOC/SOH monitoring (simple)].

Among the above-mentioned benefits, additional explanations of 2) are as follows. The main issue to ensure improved SOC/SOH monitoring is to complete correct parameter identification in the EECM. Based on minimized cell-to-cell voltage/SOC variances, it is expected to simplify EECM relations between a unit cell and battery pack, for example, the definition of the magnitude in model parameters dependent on the number of cells when considered in identical structure of the EECM. Under the final model structure and its parameter identification through simplified EECM relations, there will be absolutely no problem in accomplishing high-accuracy SOC/SOH of the battery pack.

V. Conclusion

This article provides insight into the design and implementation of the two-step HNN-based pattern recognition in order to provide the clear distinction for lithium-ion cells having similar electrochemical characteristics. For this goal, this research basically combined the DWT-based MRA into the HNN. Then, two patterns such as the DCCS and DCVS are properly used as representative patterns in the first- and second-step HNN. The role of the DWT-based MRA is to decompose the DCCS into two frequency components (approximation A_5/detail D_5) used as information on 26 characteristic parameters in the first-step HNN. After this step implementation, the identification of the representative DCCS that most closely matches that of the arbitrary DCCS is necessary. In contrast to the first-step HNN, there is no position for the DWT-based MRA in the second-step HNN. But, the final selected DCCS pattern in the previous step and its current scale adjustment should be checked since this is an important information for obtaining various DCVS patterns. The remaining procedure of the second-step HNN is the same as that of the first-step HNN. Of course, this step also considers seven characteristic parameters based on the DV/CVe patterns (current information) which were applied. The final selection of the representative DCVS pattern that is closest to an arbitrary DCVS pattern is accomplished. The similarity comparisons in parameters' magnitude in EECM such as the discharge capacity and the DCIR between 15 representative DCVSs and an arbitrary DCVS patterns definitely provide the verification of high-fidelity lithium-ion cell distinction. Compared to conventional studies, in terms of simplicity (uncomplicated), correct SOC/SOH monitoring, high-efficiency, and solution for stable battery configuration in the BMS, this research sufficiently provides useful advantages for battery users.

References

[1] H. Zhang, Y. Wang, H. Qi, and J. Zhang, "Active battery equalization method based on redundant battery for electric vehicles," *IEEE Trans. Veh. Technol.*, vol. 68, no. 8, pp. 7531–7543, Aug. 2019.

[2] S. M. Chowdhury, M. O. Badawy, Y. Sozer, and J. A. De Abreu Garcia, "A novel battery management system using the duality of the adaptive droop control theory," *IEEE Trans. Ind. Appl.*, vol. 55, no. 5, pp. 5078–5088, Sep./Oct. 2019.

[3] D. Wang, B. Nahid-Mobarakeh, and A. Emadi, "Second harmonic current reduction for a battery-driven grid interface with three-phase dual active bridge DC-DC converter," *IEEE Trans. Ind. Electron.*, vol. 66, no. 11, pp. 9056–9064, Nov. 2019.

[4] R. Xiong, Q. Yu, W. Shen, C. Lin, and F. Sun, "A sensor fault diagnosis method for a lithium-ion battery pack in electric vehicles," *IEEE Trans. Power Electron.*, vol. 34, no. 10, pp. 9709–9718, Oct. 2019.

[5] W. Gao, Y. Zheng, M. Ouyang, J. Li, X. Lai, and X. Hu, "Micro-short-circuit diagnosis for series-connected lithium-ion battery packs using mean-difference model," *IEEE Trans. Ind. Electron.*, vol. 66, no. 3, pp. 2132–2142, Mar. 2019.

[6] Y. Zheng, W. Gao, M. Ouyang, L. Lu, L. Zhou, and X. Hu, "State-of-charge inconsistency estimation of lithium-ion battery packs using mean-difference model and extended Kalman filter," *J. Power Sources*, vol. 383, pp. 50–58, Apr. 2018.

[7] S.-W. Lee, K.-M. Lee, Y.-G. Choi, and B. Kang, "Modularized design of active charge equalizer for Li-ion battery pack," *IEEE Trans. Ind. Electron.*, vol. 65, no. 11, pp. 8697–8706, Nov. 2018.

[8] D. J. Docimo and H. K. Fathy, "Analysis and control of charge and temperature imbalance within a lithium-ion battery pack," *IEEE Trans. Control Syst. Technol.*, vol. 27, no. 4, pp. 1622–1635, Jul. 2019.

[9] J. Kim, S. Lee, and B. H. Cho, "Complementary cooperation algorithm based on DEKF combined with pattern recognition for SOC/capacity estimation and SOH prediction," *IEEE Trans. Power Electron.*, vol. 27, no. 1, pp. 436–451, Jan. 2012.

[10] J. Kim and B. H. Cho, "Pattern recognition for temperature-dependent state-of-charge/capacity estimation of a Li-ion cell," *IEEE Trans. Energy Convers.*, vol. 28, no. 1, pp. 1–11, Mar. 2013.

[11] Y. Ma, P. Duan, Y. Sun, and H. Chen, "Equalization of lithium-ion battery pack based on fuzzy logic control in electric vehicle," *IEEE Trans. Ind. Electron.*, vol. 65, no. 8, pp. 6762–6771, Aug. 2018.

[12] J. Kim, J. Shin, C. Chun, and B. H. Cho, "Stable configuration of a Li-ion series battery pack based on a screening process for improved voltage/SOC balancing," *IEEE Trans. Power Electron.*, vol. 27, no. 1, pp. 411–424, Jan. 2012.

[13] L. Chen, N. Tokuda, and A. Nagaim, "Capacity analysis for a two-level decoupled Hamming network for associative memory under a noisy environment," *Neural Netw.*, vol. 20, no. 5, pp. 598–609, Jul. 2007.

[14] I. Meilijon, E. Ruppin, and M. Sipper, "A single-iteration threshold Hamming network," *IEEE Trans. Neural. Netw.*, vol. 6, no. 1, pp. 261–266, Jan. 1995.

[15] C.-K. Ngai, W. Yeung, and Z. Zhang, "Network generalized hamming weight," *IEEE Trans. Inf. Theory*, vol. 57, no. 2, pp. 1136–1143, Feb. 2011.

[16] K. Koutroumbas and N. Kalouptsidis, "Qualitative analysis of the parallel and asynchronous modes of the Hamming network," *IEEE Trans. Neural. Netw.*, vol. 5, no. 3, pp. 380–391, May 1994.

[17] J. Kim, "Discrete wavelet transform-based feature extraction of experimental voltage signal for Li-ion cell consistency," *IEEE Trans. Veh. Technol.*, vol. 65, no. 3, pp. 1150–1161, Mar. 2016.

[18] Z.-L. Zhang, X. Cheng, Z.-Y. Lu, and D.-J. Gu, "SOC estimation of lithium-ion batteries with AEKF and wavelet transform matrix," *IEEE Trans. Power Electron.*, vol. 32, no. 10, pp. 7626–7634, Jan. 2017.

[19] E. Gómez-Luna, D. Silva, G. Aponte, J. G. Pleite, and D. Hinestroza, "Obtaining the electrical impedance using wavelet transform from the time response," *IEEE Trans. Power Del.*, vol. 28, no. 2, pp. 1242–1244, Apr. 2013.

[20] C. Sen, Y. Usama, T. Carciumaru, X. Lu, and N. C. Kar, "Design of a novel wavelet based transient detection unit for in-vehicle fault determination and hybrid energy storage system," *IEEE Trans. Smart Grid*, vol. 3, no. 1, pp. 422–433, Mar. 2012.

[21] K. L. V. Iyer, X. Lu, Y. Usama, V. Ramakrishnan, and N. C. Kar, "A twofold Daubechies-wavelet-based module for fault detection and voltage regulation in SEIGs for distributed wind power generation," *IEEE Trans. Ind. Electron.*, vol. 60, no. 4, pp. 1638–1651, Apr. 2013.

[22] A. Bouzida, O. Touhami, R. Ibtiouen, A. Belouchrani, M. Fadel, and A. Rezzoug, "Fault diagnosis in industrial machines through discrete wavelet transform," *IEEE Trans. Ind. Electron.*, vol. 58, no. 9, pp. 4385–4395, Sep. 2011.

[23] M. Riera-Guasp, J. A. Antonino-Daviu, J. Roger-Folch, and M. P. M. Palomares, "The use of the wavelet approximation signal as a tool for the diagnosis of rotor bar failures," *IEEE Trans. Ind. Appl.*, vol. 44, no. 3, pp. 716–726, May/Jun. 2008.

[24] S. Lee and X. Hu, "Discrete wavelet transform-based denoising technique for advanced state-of-charge estimator of a lithium-ion battery in electric vehicles," *Energy*, vol. 83, pp. 462–473, Apr. 2015.

[25] H. Choi and J. Jeong, "Despeckling images using a preprocessing filter and discrete wavelet transform-based noise reduction technique," *IEEE Sens. J.*, vol. 18, no. 8, pp. 3131–3139, Apr. 2018.

[26] A. A. Hossam Eldin and M. A. Refaey, "A novel algorithm for discrimination between inrush current and internal faults in power transformer differential protection based on discrete wavelet transform," *Elect. Power Syst. Res.*, vol. 81, pp. 19–24, Jan. 2011.
[27] M. Riera-Guasp, J. A. Antonino-Daviu, M. Pineda-Sanchez, R. Puche-Panadero, and J. Perez-Cruz, "A general approach for the transient detection of slip-dependent fault components based on the discrete wavelet transform," *IEEE Trans. Ind. Electron.*, vol. 55, no. 12, pp. 4167–4180, Dec. 2008.
[28] C.-Y. Chun, B. H. Cho, and J. Kim, "Covariance controlled state-of-charge estimator of $LiFePO_4$ cells using a simplified hysteresis model," *Electrochim. Acta*, vol. 265, pp. 629–637, Mar. 2018.

Seongjun Lee (Member, IEEE) received the B.S. degree in electrical engineering from Kwangwoon University, Seoul, South Korea, in 2004, and the M.S. and Ph.D. degrees from Seoul National University (SNU), Seoul, South Korea, in 2006 and 2011, respectively.

From 2011 to 2016, he worked as a Senior Research Engineer with Samsung Techwin and Hyundai Mobis. He is currently an Assistant Professor with Department of Mechanical Engineering, Chosun University, Gwangju, South Korea. His main research interests include modeling and control of power conversion units for renewable energy systems/electric vehicles and control and estimation (SOC/SOH) for battery management system (BMS).

Jonghoon Kim (Senior Member, IEEE) received the B.S. degree from Chungnam National University, Daejeon, South Korea, in 2005, and the Ph.D. degree in electrical engineering and computer science from Seoul National University, Seoul, South Korea, in 2012.

From 2012 to 2013, he was a Senior Research Engineer with the Energy Storage System Development Group, Energy Solution Division, Samsung SDI, Cheonnan, South Korea. From 2013 to 2016, he was an Assistant Professor with Department of Electrical Engineering, Chosun University, Gwangju, South Korea. Since 2016, he has been an Associate Professor with Department of Electrical Engineering, Chungnam National University, Daejeon, South Korea. Since 2018, he has been an Adjunct Professor with Eco-Friendly Smart Car Research Center, Korea Advanced Institute of Science and Technology (KAIST), Daejeon, South Korea. His main research interests include battery management system (SOx estimation, prediction algorithms, equalization, and screening), next generation battery (lithium–air battery, lithium–sulfur battery, vanadium redox flow battery, solid-state battery, aluminum-ion battery, and sodium-ion/sulfur batteries), xEV retired battery (second-use), energy storage system (ESS), fault diagnosis, thermal management, artificial intelligence, power electronics circuits, and fuel cell system (ripple current analysis and energy management system).

Dr. Kim is a member of the IEEE Power Electronics, Industrial Electronics, Power & Energy, Vehicular Technology, Transportation Electrification, and Industry Application Societies, and the Korean Institute of Power Electronics, the Korean Institute of Electrical Engineers, the Korean Society of Automotive Engineers, the Korean Electrochemical Society, the Institute of Electronics and Information Engineers, and the Korean Society for Aeronautical and Space Sciences. Since 2015, he has been an Associate Editor for the *Journal of Power Electronics (JPE)*. Since 2019, he has been an Associate Editor for the *IEEE Access* and Topic Editor for the *MDPI Electronics*. He was the recipient of the Student Paper Award at the *2010 International Power Electronics Conference (IPEC-10)*.